scientific reports

OPEN

Ground subsidence monitoring and analysis of Lairong railway during its entire construction cycle based on SBAS-InSAR

Feng Sheng[1,2], Long Chai[3], Xingchang Zhang[2], Jiangtao Wu[2], Li Ma[2], Kaisong Geng[2], Qiming Han[2], Xiongyao Xie[3] & Xiaoqing Zeng[4]✉

Ground subsidence poses a significant threat to the structural stability and operational safety of railway systems, highlighting the critical need for effective monitoring throughout the construction lifecycle. Subsidence monitoring data along railway alignments can be leveraged to analyze subsidence characteristics across different sections and to track time-series deformation at specific locations. This study proposes a comprehensive framework for the spatio-temporal analysis of subsidence along railway lines, grounded in the Small Baseline Subset Interferometric Synthetic Aperture Radar (SBAS-InSAR) technique. To this end, 39 Sentinel-1 A SAR images were processed to derive subsidence data spanning the pre-construction, construction, and post-construction phases of the Lai-Rong Railway, with results validated against ground leveling measurements. Hotspot analysis was employed to identify subsidence clustering zones, while time-series deformation, average cumulative subsidence, and correlation coefficients were utilized to examine spatio-temporal patterns at targeted locations. The findings demonstrate that SBAS-InSAR achieves millimeter-level accuracy in subsidence monitoring, revealing an uneven spatial distribution along the railway. Notably, the DK30 ~ DK50 section exhibited substantially higher subsidence rates, primarily attributed to large-scale crustal deformation. Construction activities, such as ground excavation, leveling, and load introduction, emerged as primary drivers of subsidence, particularly in surface fill soils. To mitigate long-term subsidence risks, thorough compaction of fill layers is recommended, along with increased monitoring frequency in high-risk sections to enhance safety. This study offers valuable insights into the application of SBAS-InSAR for ground subsidence monitoring across the full construction cycle of large-scale railway projects.

Keywords High-speed railway, Ground subsidence, SBAS-InSAR, Spatio-temporal analysis

By the end of 2023, the total railway mileage in mainland China reached 159,000 km, making it the second-largest network globally. The North China Plain (NCP), one of China's three major plains, spans Beijing, Tianjin, Hebei, Shandong, Henan, Anhui, and Jiangsu provinces and municipalities. The region is characterized by a high population density, a developed economy, and a relatively sparse railway network[1]. However, since the 1970 s, the NCP has experienced severe ground subsidence from extensive groundwater extraction, leading to the formation of multiple subsidence centers that are expanding and merging into larger areas[2,3]. Railways, as long-distance linear infrastructure, consist of various components[4–6], including stations, pavements, bridges, tunnels, embankments, and tracks. Ground subsidence poses significant challenges to railway infrastructure, causing structural damage such as pavement cracking, collapses, differential settlement of bridges, track irregularities, and deformation of precast beams in beam yards[7,8]. It can also induce geological hazards, such as slope instability near tunnel entrances and exits or along railway routes, posing risks to railway operations[9]. Moreover, planned railway routes often intersect with existing highways, railways, and residential areas, which are highly susceptible to the impacts of subsidence[10,11]. Consequently, monitoring ground subsidence along railway lines is critical for ensuring project safety.

[1]School of Civil Engineering, Tsinghua University, Beijing 100084, China. [2]Powerchina Roadbridge group co.,LTD, Beijing 100160, China. [3]Department of Geotechnical Engineering, College of Civil Engineering, Tongji University, Shanghai 200092, China. [4]The Key Laboratory of Road and Traffic Engineering Ministry of Education, Tongji University, Shanghai 201804, China. ✉email: zengxq@tongji.edu.cn

| https://doi.org/10.1038/s41598-025-20718-y

The monitoring data enable the identification of areas with significant subsidence and the analysis of temporal subsidence trends at specific locations, thereby providing essential insights for railway construction and informed decision-making. Traditional methods for monitoring railway ground subsidence, such as leveling, total station monitoring, terrestrial laser scanning, and GPS[12–14], provide high precision but are limited by low spatial resolution, high measurement costs, and challenges in maintaining equipment for high-speed railway projects. Interferometric Synthetic Aperture Radar (InSAR) is a powerful technique for measuring ground deformation, with advantages including high observation frequency, cost-effectiveness, and access to historical data archives. InSAR was initially developed for measuring ground elevation, with the capability to achieve meter-level measurement precision[15]. Subsequently, Differential InSAR (D-InSAR) was proposed for measuring large-scale ground deformation and was successfully applied to earthquake deformation monitoring, landslide deformation analysis, and other crustal activity monitoring, with deformation measurement precision reaching the centimeter level[16–18]. However, D-InSAR is susceptible to atmospheric delays and temporal-spatial decorrelation, which can introduce errors to results[19]. Multi-Temporal InSAR (MT-InSAR) techniques, such as Persistent Scatterer InSAR (PS-InSAR) and Small Baseline Subset InSAR (SBAS-InSAR), have been developed to address these limitations[20,21]. These methods achieve millimeter-level precision in deformation monitoring by analyzing the phase differences of stable pixels across multiple SAR images. Specifically, PS-InSAR identifies pixels on SAR images that maintain stable reflection intensity and phase over time, known as Persistent Scatterers (PSs), which typically correspond to artificial structures like buildings and bridges, or to natural features such as exposed rocks. In contrast, SBAS-InSAR generates interferograms from SAR image pairs using small temporal and spatial baselines, creating a dense network that minimizes decorrelation and enables the analysis of distributed scatterers across broader areas, including regions with moderate vegetation or seasonal changes. MT-InSAR has been successfully applied in ground subsidence monitoring[22], the identification and assessment of geological hazards[23,24], the risk identification of urban buildings[25,26], the management of heritage conservation[27], and infrastructure deformation monitoring[28–30], among other applications. In the context of infrastructure, given the significant challenges posed by ground subsidence to railway systems, many studies have employed MT-InSAR to investigate ground subsidence along railway lines and the deformation of railway structures. There are several research hotspots:

(1) Monitoring ground subsidence along railway lines. SBAS-InSAR is utilized to monitor ground subsidence along railway line, integrating geological conditions and other factors to analyze the underlying causes of subsidence[31,32]. (2) Monitoring deformation of railway structures. MT-InSAR is used to continuously monitor railway structural components, such as bridges, slopes, and tunnels[33–35], providing detailed insights into their deformation behavior over time. (3) Enhancement of InSAR algorithms and application scenarios. Some studies have focused on railways to enhance time series InSAR algorithms[36,37], introducing improvements that increase the accuracy and applicability of these methods for railway monitoring. (4) Integration of complementary data and techniques. Some studies have integrated complementary data and techniques, such as LiDAR point cloud data and GPR, to further improve the precision of deformation monitoring in railway project[38,39]. (5) Integration of MT-InSAR with machine learning. Some studies combine MT-InSAR with machine learning for the analysis of ground subsidence along railway lines under multiple influencing factors[40].

Railways often traverse low-coherence areas, where SBAS-InSAR typically outperforms PS-InSAR in monitoring ground subsidence along railway lines. PS-InSAR can identify persistent scatterers (PSs) associated with the railway after its construction is complete, making it more suitable for monitoring operational railway structures. Despite the numerous successful applications of MT-InSAR in railway monitoring, current research has notable limitations. Most studies focus on operational railways, while railways under construction have received limited attention. Furthermore, few studies have explored the use of MT-InSAR for spatiotemporal subsidence analysis along railway lines or for tracking the deformation characteristics of specific components across various construction stages. To address these gaps, this study proposes a SBAS-InSAR-based method for analyzing and evaluating ground subsidence along railway lines during construction. The method is applied to the Shandong Lairong high-speed railway project to investigate the spatiotemporal evolution of ground subsidence along the railway during different construction stages.

This study advances railway subsidence monitoring by integrating SBAS-InSAR with hotspot analysis to characterize the spatial distribution and clustering of deformation along railway lines, incorporating a sensitivity analysis for optimal fixed-band distance selection based on Chinese railway standards. Furthermore, SBAS-InSAR time-series data are combined with construction timelines at critical structures, such as beam yards, bridge, and tunnel entrances, to detect sudden subsidence changes during construction and quantify pattern shifts via correlation coefficients across different construction phases. Subsidence is primarily attributed to miscellaneous fill layer compression rather than bedrock deformation, supported by empirical evidence from prior studies. The paper is structured as follows: The introduction outlines the research significance and objectives. Section 2 describes the study area, including project overview and SAR data. Methodology in Sect. 3 details SBAS-InSAR for ground subsidence monitoring, along with visualization and analysis in ArcGIS, incorporating engineering data and subsidence indicators. Results in Sect. 4 cover SBAS-InSAR data processing, monitoring outcomes, spatiotemporal evolution analysis via hotspot methods, and time-series deformation at key nodes. Discussion in Sect. 5 evaluates the advantages and limitations of SBAS-InSAR. Moreover, spatiotemporal patterns and deformation trends of ground subsidence along the railway are discussed. Finally, conclusions summarize key findings and implications.

Study area and data

Project overview

The Lairong Railway is situated in the southeastern coastal region of the Jiaodong Peninsula, Shandong Province. The route traverses gently undulating eroded hills and plains with natural slopes ranging from 10° to

25°, characterized by dense vegetation, as depicted in Fig. 1, which illustrates the terrain and landforms along the railway. Influenced by regional fault zones, the geological structure comprises Quaternary Holocene deposits, including gravelly sands, silty sandstone, and shale, underlain by stable bedrock. Geotechnical evaluations indicate a continuous stratigraphic distribution and high bearing capacity, particularly in moderately weathered granite and andesite, supporting construction. Seismic analyses reveal low peak ground acceleration and compliance with high seismic fortification standards, ensuring safety against seismic activities. Additionally, soil corrosion assessments show mild corrosiveness toward concrete structures, suggesting minimal impact on long-term structural stability. Collectively, these favorable geological, geotechnical, and seismic conditions make this region highly suitable for large-scale construction projects.

Section I of the Lairong Railway extends from Laixi Station to Haiyang Station, spanning a main line length of 69.76 km with a design speed of 350 km/h. To cross existing infrastructure, such as the Wei-Qing Expressway, and traverse regions including the Wulong River and towns like Haiyang, large-scale bridge construction is essential. To facilitate this, two beam fabrication yards have been strategically established along the route to support bridge construction. Additionally, the railway's alignment through hilly terrain with significant elevation variations requires tunnels in specific segments to ensure efficient traversal. Figure 2 illustrates the railway's starting and ending points, highlighting key nodes and structural forms along the route.

SAR data
The SAR images utilized in this study are Sentinel-1 A Single Look Complex (SLC) images, acquired from the European Space Agency. Sentinel-1 A, equipped with a C-band radar, provides medium-resolution data with a 12-day revisit cycle. In this study, 39 SLC SAR images covering the railway project area were collected from July 29, 2020, to May 27, 2023. Additionally, precise orbit data from Sentinel satellites were used to mitigate orbit errors. The detailed parameters of the Sentinel-1 A images are presented in Table 1.

Methodology
The workflow of the proposed methodology is shown in Fig. 3. It begins with the application of SBAS-InSAR to detect deformation along the railway alignment. The detected Line of Sight (LOS) deformation is then converted into the vertical direction to enable more intuitive analysis of ground deformation. A buffer zone is subsequently established along the railway alignment, within which spatiotemporal analysis is conducted to identify regions with significant settlement changes. Following this, time series analysis is applied to monitor and track deformation at critical structural locations over time, providing detailed insights into the temporal evolution of deformation patterns.

Ground subsidence monitoring along railway by SBAS-InSAR
The SBAS-InSAR method is founded on the principle of employing small baseline subsets to estimate the deformation rate of a region. The process begins by setting time and spatial baseline thresholds to guide the selection of interferometric pairs. For a set of $N + 1$ SAR images, the method divides these images into L subsets,

Fig. 1. The terrain and landforms along the railway.

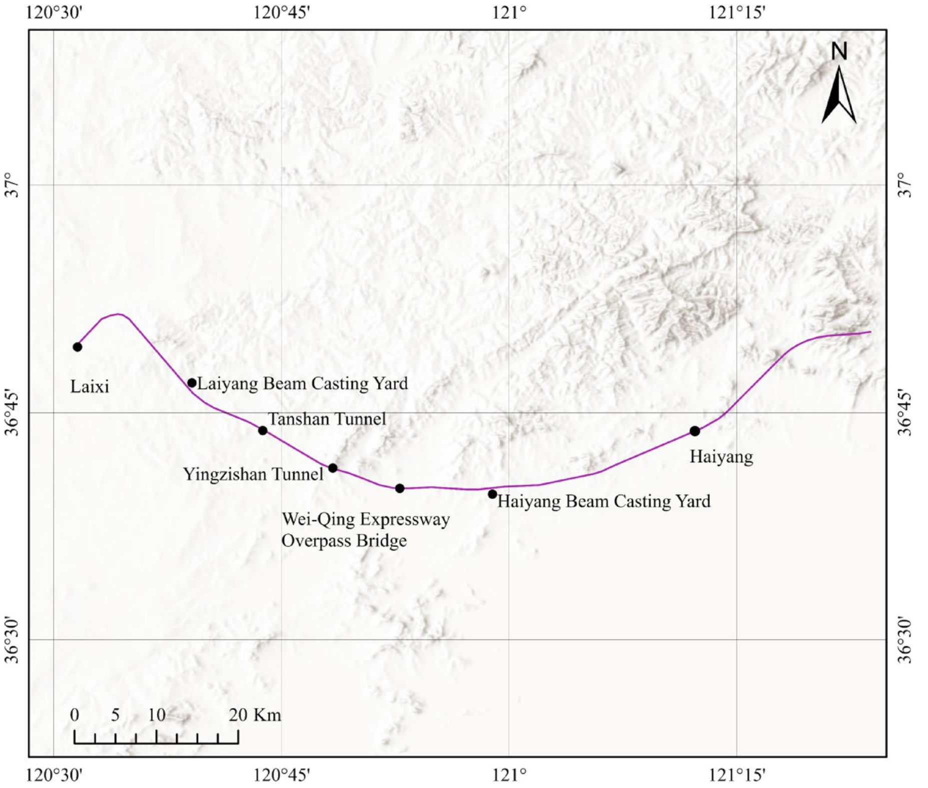

Fig. 2. Route and key nodes the Lairong Railway. The Figure is generated by ArcGIS (https://www.esri.com/en-us/arcgis/products/arcgis-pro/resources), and the map used is World Hillshade (https://services.arcgisonline.com/arcgis/rest/services/Elevation/World_Hillshade/MapServer).

Sentinel-1 A	Parameters
Date	2020.07.29–2023.05.27
Incidence Angle	20° – 46°
Polarization Mode	Single Polarization (VV)
Acquisition Mode	IW Mode
Orbit	Ascending
Wavelength	C band (5.6 cm)
Resolution	2.7 × 22 – 3.5 × 22/m×m
Data Format	Single Look Complex (SLC)

Table 1. Parameters of Sentinel-1 A.

where each subset satisfies the criteria of small time and spatial baselines, while larger baselines are maintained between different subsets. After interferometric processing, M interferometric pairs are generated[21,41]:

$$\frac{(N+1)}{2} \leqslant M \leqslant (N+1) \tag{1}$$

Following the registration and interferometric processing of two SAR images, the differential interferometric phase can be expressed as:

$$\delta\phi(T) = \phi(t_A) - \phi(t_B) \approx \delta\phi_{disp} + \delta\phi_{topo} + \delta\phi_{atmo} + \delta\phi_{noi} \tag{2}$$

where $\delta\phi(T)$ is the differential interferometric phase;
$\phi(t_i)$ is the phase to be determined on the i-th image;
$\delta\phi_{disp}$ is the deformation phase;
$\delta\phi_{topo}$ is the topographic phase;
$\delta\phi_{atmo}$ is the atmospheric phase;
$\delta\phi_{noi}$ is the noise phase.

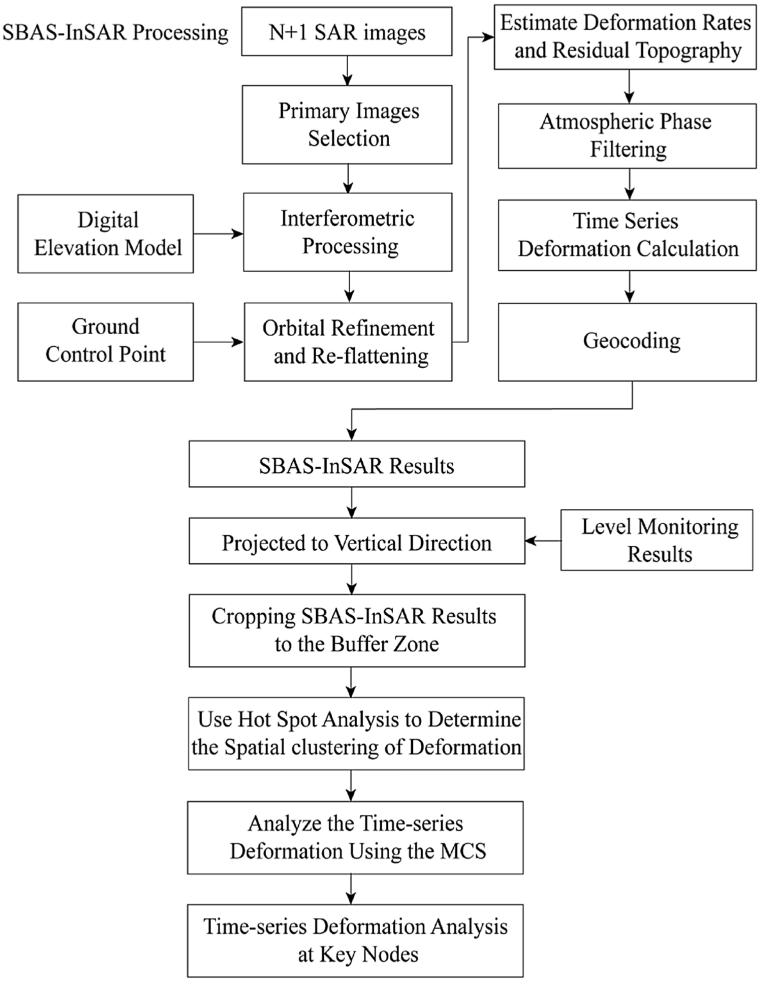

Fig. 3. The workflow of the proposed methodology.

In the SBAS-InSAR methodology, after removing decorrelation, elevation errors, and atmospheric delays, the differential interferometric phase due to ground deformation is expressed as

$$\delta\phi(T) \approx \delta\phi_{disp} = \frac{4\pi}{\lambda}[d_{t_A} - d_{t_B}] \tag{3}$$

Where λ is the radar wavelength;

d_{t_A} and d_{t_B} represent the LOS deformations relative to the initial time.

The differential interferometric phase is treated as the observed quantity, form a system of M equations with N unknowns. This system can be expressed in matrix form as:

$$A\phi = \delta\phi \tag{4}$$

where A is an $M \times N$ incidence matrix, with each row corresponding to an interferogram pair and each column to a SAR acquisition date. Singular value decomposition is applied to solve this system, yielding the phase time series ϕ. The deformation velocities between consecutive acquisitions are then computed and integrated to obtain the cumulative deformation time series.

However, the phase time series often contains non-deformation signals, such as elevation errors, atmospheric delays, and noise. To address this, SBAS-InSAR employs polynomial modeling to mitigate low-frequency deformation and elevation errors, followed by temporal high-pass filtering to remove atmospheric delay and orbital errors. This process produces the deformation phase sequence of coherent targets. Finally, the line-of-sight (LOS) time series deformation is projected onto the vertical direction using the following formula:

$$S_{v,i} \approx \frac{S_{LOS,i}}{\cos\theta_i} \tag{5}$$

where $S_{v,i}$ is the vertical deformation of the i-th pixel;

$S_{LOS,i}$ is the line-of-sight deformation of the i-th pixel;

θ_i is the local incidence angle of the of the i-th pixel.

SBAS-InSAR results visualization and analysis

Visualization of SBAS-InSAR ground subsidence results with engineering data in ArcGIS

First, integrate the SBAS-InSAR subsidence results and engineering project data into ArcGIS. Then, ensure the engineering project data include a railway shapefile with essential details, such as the railway alignment, locations of structural components and leveling points for validation. Next, project both datasets into a unified geographic coordinate system to ensure spatial consistency.

Subsequently, create a buffer zone around the railway alignment to define the spatial extent for subsidence analysis.

Afterwards, clip the SBAS-InSAR subsidence data to this buffer zone to isolate deformation patterns associated with the railway line. Finally, generate the subsidence map of the railway line by visualizing the clipped SBAS-InSAR results.

Ground subsidence analysis indicators

Mean cumulative subsidence is used as an indicator to analyze the overall ground subsidence level at a specific point in time.

$$S_{MCS} \approx \sum_{i=1}^{N} S_i \Big/ N \tag{6}$$

Where S_{MCS} is the mean cumulative subsidence of the study area;

S_i is the cumulative subsidence of the i-th pixel;

N is the total number of pixels.

Ground subsidence velocity difference is used to assess the severity of ground subsidence in a specific area relative to the overall region during the same period.

$$V_{all} = \frac{S_{all}^{t_1} - S_{all}^{t_2}}{t_1 - t_2} \tag{8}$$

$$V_i = \frac{S_i^{t_1} - S_i^{t_2}}{t_1 - t_2} \tag{9}$$

Where V_{diff} is the subsidence velocity difference;

V_{all} represents the mean ground subsidence velocity of the entire region during the time period from t_1 to t_2;

$S_{all}^{t_1}$ and $S_{all}^{t_2}$ are the mean cumulative subsidence values for the entire region at timest_1 and t_2, respectively;

$S_i^{t_1}$ and $S_i^{t_2}$ are the subsidence values for the specific area i at times t_1 and t_2, respectively.

The correlation coefficient r is a statistical measure that quantifies the strength and direction of the linear relationship between two variables[42].

$$r = \frac{\sum \left(d_{i,t} - d_{i,mean}\right)\left(d_{background,t} - d_{background,mean}\right)}{\sqrt{\sum \left(d_{i,t} - d_{i,mean}\right)^2 \sum \left(d_{background,t} - d_{background,mean}\right)^2}} \tag{10}$$

$d_{i,t}$ is the deformation at the i-th point at time t;

$d_{i,mean}$ is the mean deformation of the i-th point over the time period;

$d_{background,t}$ is the MCS of the entire study area at time t;

$d_{background,mean}$ is the mean MCS of the entire study area over the time period.

The correlation coefficient ranges from −1 to 1. Values approaching 1 indicate a strong positive linear relationship between deformation patterns, values nearing −1 suggest a strong negative linear relationship, and values close to 0 indicate little to no linear relationship between the deformation patterns.

Results

SBAS-InSAR data processing

In this study, the SAR images were cropped to enhance data processing efficiency. The SBAS-InSAR consists of the following key steps:

(1) Connection graph generation. The optimal master image, selected based on factors such as the Doppler effect and spatiotemporal baselines, was determined to be the image from May 25, 2021, as shown in Fig. 4. The time baseline was set with a minimum of 0 days and a maximum of 180 days. The critical baseline was defined with a minimum of 0% and a maximum of 2%. This step forms the basis for the interferometric pair selection.

(2) Interferometric processing. Based on the connection graph, all images were co-registered to the master image. This was followed by interferometric processing, which included filtering, flattening, and phase unwrapping. For coherence management, both the unwrapping and product coherence thresholds were set to 0.3 to exclude low-coherence areas and enhance overall data quality. The Goldstein filter was applied for adaptive noise reduction while preserving phase details subsequently. Finally, the minimum cost flow unwrapping method was employed to robustly minimize unwrapping errors.

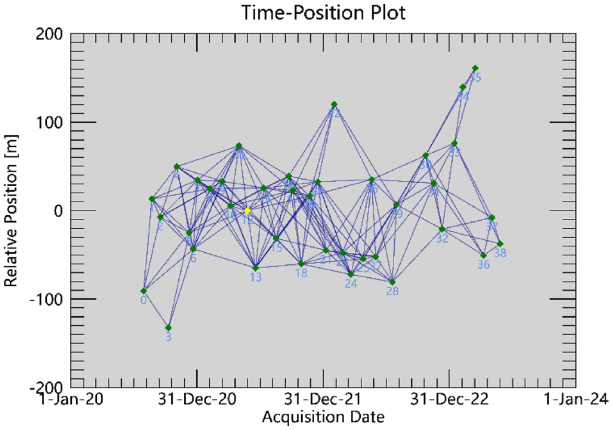

Fig. 4. Spatiotemporal baseline graph.

(3) Orbital refinement and re-flattening. Using the unwrapped phases obtained from Step 2, ground control points were selected in areas with minimal deformation and reliable unwrapping results. Polynomial methods were applied to flatten the interferograms further, ensuring accurate deformation analysis.

(4) Deformation inversion. From the refined results of Step 3, the deformation rate and residual topography were estimated. A high-pass filter with a spatial cutoff of 1200 m was applied to remove large-scale low-frequency noise, such as atmospheric effects and orbital errors, while a low-pass filter with a temporal cutoff of 365 days was used to smooth high-frequency temporal noise, including short-term fluctuations, and extract long-term deformation trends essential for accurate subsidence monitoring.

(5) Geocoding. The deformation results obtained in Step 4 were transformed from SAR coordinate space into geographic coordinates, enabling spatial analysis in real-world mapping systems.

(6) Vertical Deformation Calculation. Finally, all line-of-sight (LOS) deformation measurements derived in Step 5 were converted into the vertical direction.

Ground subsidence monitoring results by SBAS-InSAR

ArcGIS, an effective geographic information system (GIS) platform, facilitates the visualization of engineering data and SBAS-InSAR ground subsidence results. Figure 5 shows the vertical ground deformation monitoring results derived from SBAS-InSAR across the study area, depicted using a color gradient in millimeters per year (mm/a), ranging from red to dark green. Red regions indicate significant subsidence, orange to yellow areas denote moderate subsidence, light green areas reflect near-stability or slight subsidence, and dark green regions signify uplift. The deformation characteristics of the study area show that the eastern and western regions are relatively stable, with minor deformation velocities, primarily slight subsidence or uplift, while the central and northeastern regions exhibit more significant deformation, with higher velocities dominated by subsidence. The railway section from DK30 to Haiyang Station lies within these central and northeastern regions, where significant subsidence is observed.

In this study, the buffer zone radius was set to 1 km, based on the following considerations: (1) According to the Railway Safety Management Regulations of the People's Republic of China and the High-Speed Railway Safety Protection Measures, a 1-km zone on both sides of the railway is designated as the safety protection zone. (2) Previous studies indicate that a 1-km buffer radius accounts for the typical propagation range of subsidence influences, such as soil compression from pile foundations or tunneling and geotechnical hazards like groundwater extraction[43–45]. (3) The maximum distance from the auxiliary engineering structures of the Lai-Rong Railway to the railway centerline is approximately 900 m. Therefore, considering both the impact range of railway construction and the safety protection zone, the buffer zone radius was finalized as 1 km. The 1-km buffer zone was established along the railway line using ArcGIS, and the SBAS-InSAR results were clipped to this zone, as shown in Fig. 6. The subsidence velocities range from – 41.14 mm/a to 23.57 mm/a, revealing significant spatial variability in ground subsidence along the railway from Laixi Station to Haiyang Station.

(1) Laixi Station to DK30: This segment primarily displays slight uplift, with deformation velocities ranging from – 1.35 mm/a to 7.15 mm/a.

(2) DK30 to DK50: This segment shows more pronounced subsidence, with velocities ranging from – 1.35 mm/a to −41.47 mm/a.

(3) DK50 to Haiyang Station: This segment also shows a subsidence trend, with generally moderate deformation velocities within – 10.58 mm/a.

During the railway construction, the leveling method was employed to monitor ground subsidence along the railway, and the resulting leveling data were used to validate the SBAS-InSAR results. Thirty leveling points were selected along the railway line from Laixi to Haiyang based on their mileage for this validation. The validation results, shown in Fig. 7, reveal a maximum difference of 8.79 mm between the two datasets, with a root mean square error (RMSE) of 3.84 mm.

Figure 8 shows some coherence maps of the SBAS-InSAR results, with the acquisition time of the SAR images and the mean coherence coefficient marked in the figure. During June to October, which is the summer

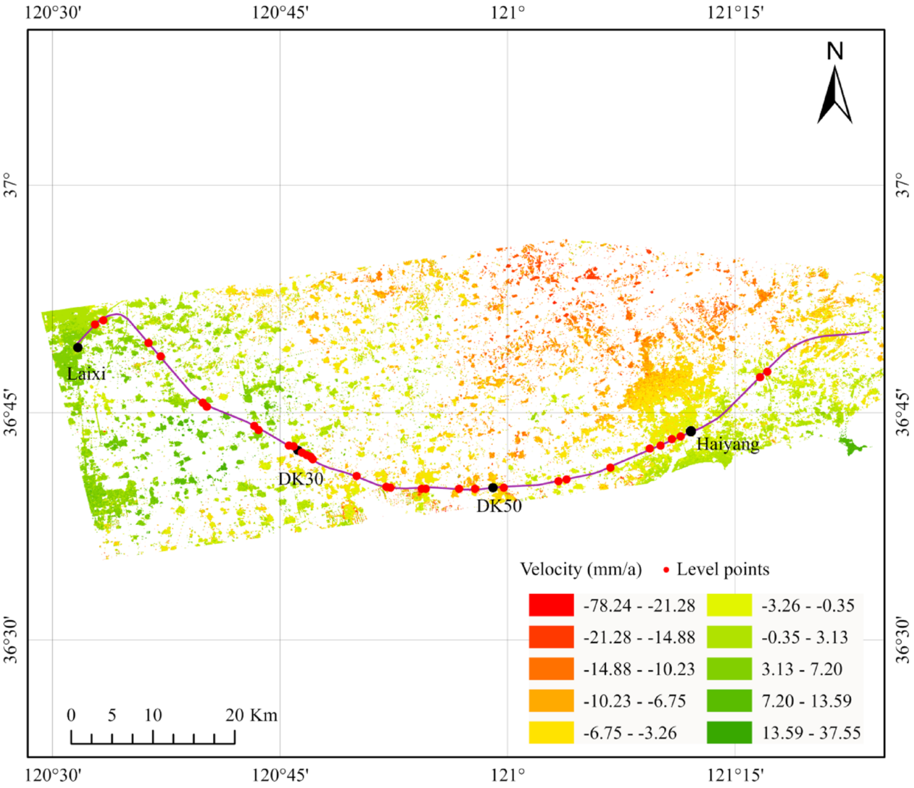

Fig. 5. SBAS-InSAR results and ground subsidence map. The Figure is generated by ArcGIS (https://www.esri.com/en-us/arcgis/products/arcgis-pro/resources), and the map used is World Hillshade (https://services.arcgisonline.com/arcgis/rest/services/Elevation/World_Hillshade/MapServer).

vegetation growth period, the coherence of interferometric pairs is lower, while from November to March, the coherence is higher. Within the 1-km buffer zone of engineering concern, the SBAS-InSAR results indicate that the mean coherence coefficient in the 1-km buffer zone is 0.50.

Spatiotemporal evolution analysis of ground subsidence along the railway

In this study, the Getis-Ord Gi* method was employed to detect spatial clustering of subsidence. Statistical significance levels were set at 0.01 and 0.05, corresponding to 99% and 95% confidence levels, respectively. Regions identified at these thresholds were deemed highly reliable. SBAS-InSAR-derived ground subsidence rates served as the input for the analysis. According to China's Code for Design of High-Speed Railway (TB 10621 – 2014)[46], the post-construction settlement of ballastless track bridge piers should not exceed 20 mm. And in railway engineering practice, a subsidence rate of 20 mm/year is typically used as the warning threshold for railway subsidence monitoring. Thus, the hotspot analysis is expected to pinpoint areas with ground deformation rates surpassing 20 mm/year. However, in the SBAS-InSAR results, the proportion of pixels exhibiting subsidence or uplift rates exceeding 20 mm/year is relatively low. To assess the influence of fixed distance bands on hotspot analysis outcomes, pixels with subsidence or uplift rates greater than 10 mm/a were first extracted from the SBAS-InSAR results. The proportion of these pixels classified as cold spots or hot spots at the 99% confidence level was then computed. A higher proportion suggests a more appropriate fixed distance band. The influence range on both sides of the railway is typically 50 m to 200 m. Therefore, the fixed distance band is set to start from 50 m and gradually increase. The identification results of pixels with deformation rates greater than 10 mm/a or less than – 10 mm/a for different distance bands are shown in Table 2. The results indicate that the 50 m fixed buffer distance performs optimally, with the highest proportion of pixels with ground deformation greater than 10 mm/a or less than – 10 mm/a correctly identified as hot spots and cold spots at the 99% confidence level.

The Getis-Ord Gi* analysis effectively delineating areas of statistically significant subsidence clustering, as shown in Fig. 9. Cold spots indicate clusters of subsidence, while hot spots represent clusters of uplift. The results reveal that areas with clustered subsidence are predominantly located between DK30 and Haiyang Station.

A detailed examination of the subsidence map from DK30 to Haiyang Station, as presented in Fig. 10, reveals that the DK30 to DK50 segment exhibits significantly more severe subsidence compared to other sections of the railway from a spatial perspective.

MCS values for each observation time were calculated separately for all pixels of the SBAS-InSAR results within the 1-km buffer zone and the DK30 ~ DK50 section to analyze the temporal evolution of subsidence in these two areas. Both curves exhibit similar patterns of deformation, characterized by gradual subsidence amidst fluctuations, as shown in Fig. 11. The fitted linear regression lines indicate a consistent downward trend in MCS

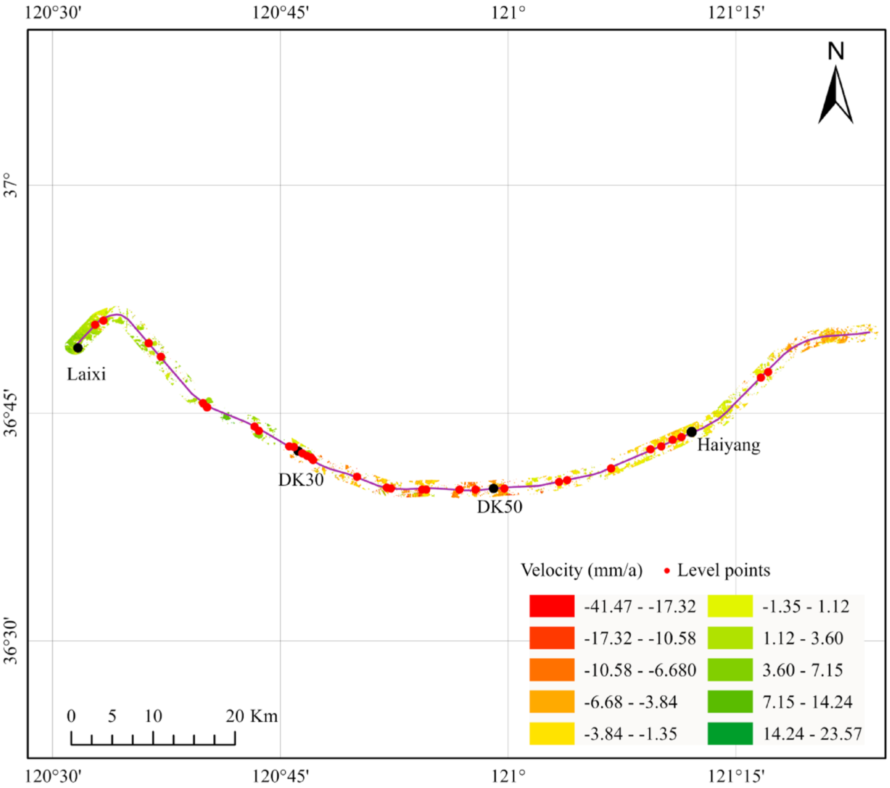

Fig. 6. SBAS-InSAR results and ground subsidence map. The Figure is generated by ArcGIS (https://www.esri.com/en-us/arcgis/products/arcgis-pro/resources), and the map used is World Hillshade (https://services.arcgisonline.com/arcgis/rest/services/Elevation/World_Hillshade/MapServer).

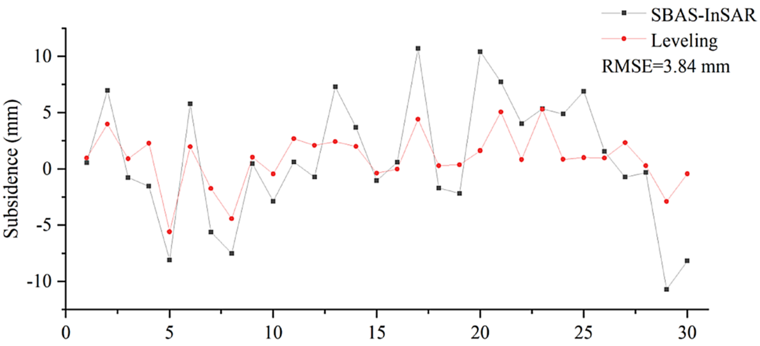

Fig. 7. Comparison of leveling measurement and SBAS-InSAR measurement results.

for both datasets. However, the DK30 ~ DK50 region displays a faster subsidence trend compared to the 1-km buffer zone.

The Lairong Railway was constructed from November 2, 2020, to November 15, 2022. Prior to construction, the DK30 ~ DK50 section exhibited significant subsidence, with a mean cumulative subsidence of 6.95 mm, while the buffer zone remained relatively stable at a mean of 3.14 mm. By November 25, 2021, one year after construction began, the DK30 ~ DK50 section's mean subsidence had increased markedly to 11.93 mm, whereas the buffer zone showed minimal change, with a mean of 2.72 mm. Upon completion of construction on December 10, 2022, the DK30 ~ DK50 section recorded a mean subsidence of 12.74 mm, and the buffer zone exhibited a moderate increase to 4.88 mm. Six months post-construction, on May 27, 2023, subsidence in the DK30 ~ DK50 section intensified further to a mean of 17.37 mm, while the buffer zone showed a slight increase to 5.01 mm.

Using time series MCS results for the buffer zone and the DK30 ~ DK50 section, the ground subsidence velocity differences between the buffer zone and the DK30 ~ DK50 section were calculated across the four monitoring periods, as shown in Table 3, covering the pre-construction, construction, and post-construction phases of the Lairong Railway. During the pre-construction period (July 29, 2020–November 2, 2020), the velocity difference was 14.53 mm/a. In the early construction phase (November 2, 2020–December 15, 2021),

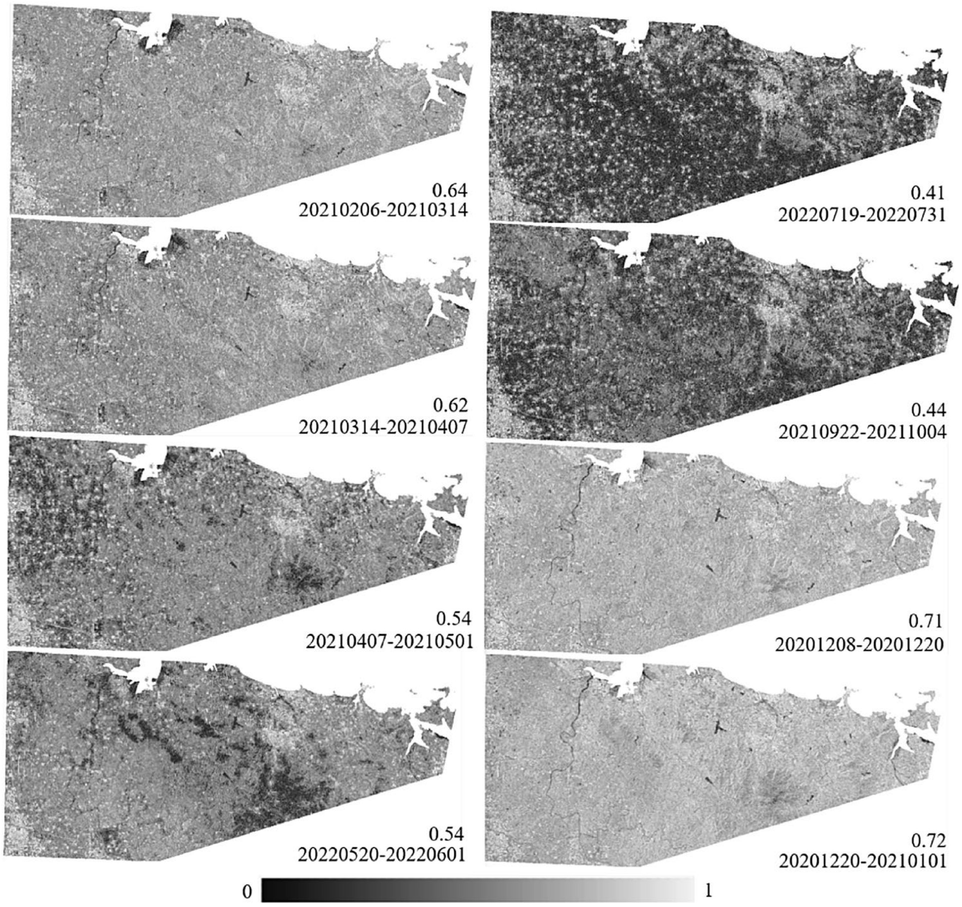

Fig. 8. Coherence maps of some interferometric pairs based on SBAS-InSAR.

Fixed distance bands (m)	Proportion of pixels classified as cold spots or hot spots at the 99% confidence level (%)	
	> 10 mm/a	< −10 mm/a
50	94.56	92.62
100	93.65	88.36
200	94.00	87.00
400	94.06	84.82
800	94.50	86.59

Table 2. The proportion of deformation pixels correctly identified as hot spots and cold spots under different distance bands.

the velocity difference decreased to 4.82 mm/a. As construction progressed (December 15, 2021–December 10, 2022), the velocity difference further reduced to 1.36 mm/a. In the post-construction period (December 10, 2022–May 27, 2023), the velocity difference increased to 9.76 mm/a.

Time series deformation analysis at key nodes

Haiyang beam yard

The Haiyang Beam Yard serves as a key auxiliary facility for the railway engineering project, supporting beam manufacturing and storage. Situated at DK51 + 000 on the right side of the railway line, it covers an area of 300 acres and comprises 18 beam manufacturing bases and 108 beam storage bases. Construction started on November 1, 2020, and concluded on May 1, 2021.

Figure 12 presents the ground subsidence velocity map for the Haiyang Beam Yard, showing elevated subsidence velocities within the yard compared to surrounding areas, while Fig. 13 presents the time series data from three pixels (locations A, B, and C) within the beam yard.

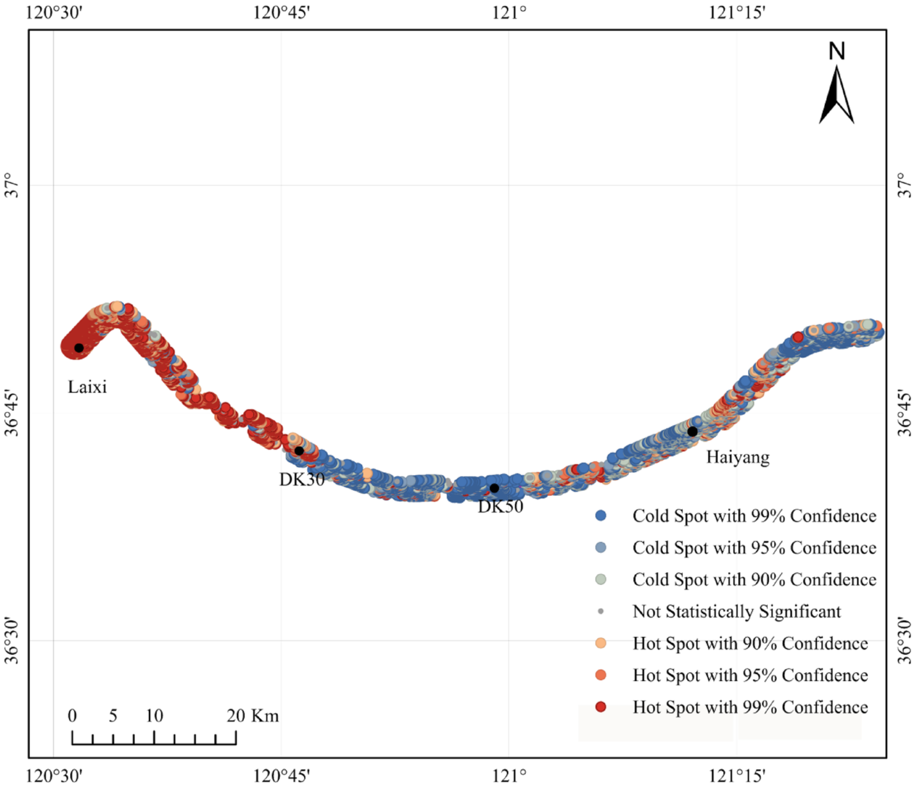

Fig. 9. The hot spot analysis results of SBAS-InSAR.

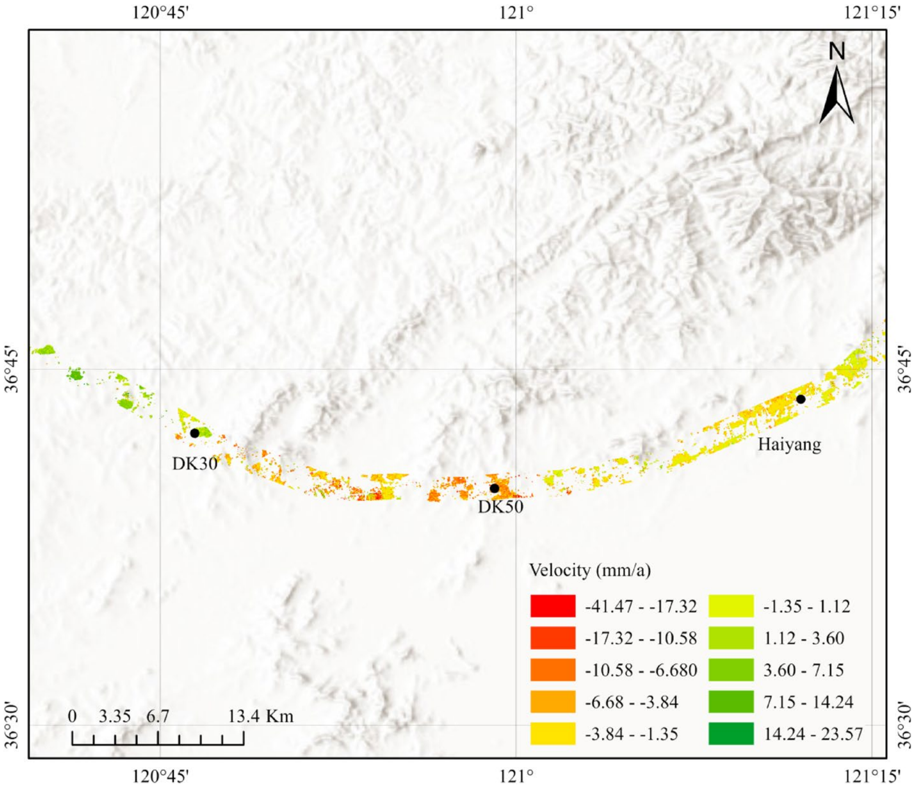

Fig. 10. Ground subsidence map (DK30 ~ Haiyang Station). The Figure is generated by ArcGIS (https://www.esri.com/en-us/arcgis/products/arcgis-pro/resources), and the map used is World Hillshade (https://services.arcgisonline.com/arcgis/rest/services/Elevation/World_Hillshade/MapServer).

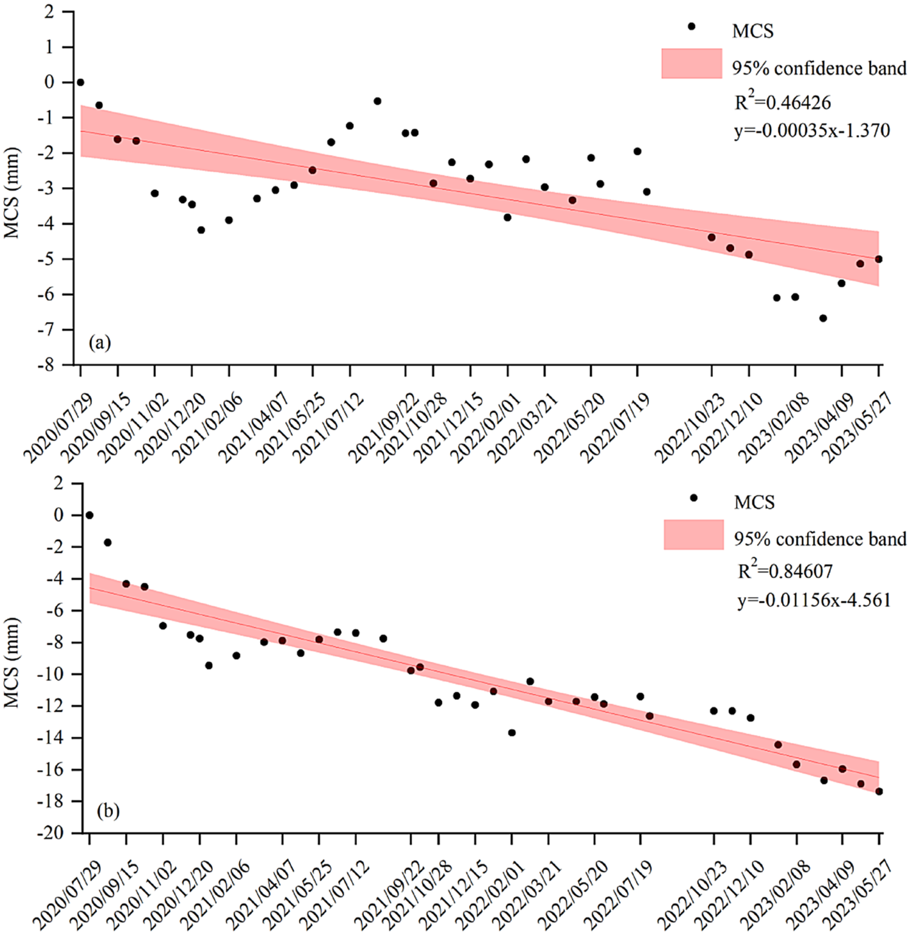

Fig. 11. Time series MCS results of the (**a**) 1 km buffer zone, (**b**) DK30 ~ DK50 section.

Monitoring period	Velocity difference (mm/a)
2020/07/29-2020/11/02	14.53
2020/11/02-2021/12/15	4.82
2021/12/15-2022/12/10	1.36
2022/12/10-2023/05/27	9.76

Table 3. Ground subsidence velocity difference between the buffer zone and DK30 ~ DK50.

At the end of the construction period (July 27, 2020 ~ May 1, 2021), cumulative subsidence at locations A, B, and C was 41.82 mm, 70.01 mm, and 28.42 mm, respectively, and ground subsidence during this period exhibited significant fluctuations. At the end of the beam production period (May 1, 2021 ~ May 20, 2022). cumulative subsidence at locations A, B, and C was 47.03 mm, 75.43 mm, and 40.60 mm, respectively. and during this period, the subsidence velocity gradually slowed. During the post-production period, subsidence velocity continued to decrease at all three locations.

Weiqing expressway grand Bridge

The Wei-Qing Expressway Grand Bridge, located at DK41 + 563 along the railway line, spans the Wei-Qing Expressway (G1813). As a continuous beam bridge, it represents a critical component of the railway project. Construction of the bridge started on February 1, 2022, and concluded on January 27, 2023. Figure 14 shows elevated subsidence velocities at the intersection of the railway and expressway. Subsidence velocities in most areas range from 3.84 mm/a to 41.47 mm/a, with higher subsidence velocities on the north side of the bridge and lower subsidence velocities on the south side.

Figure 15 presents the time series data from three locations (D, E, and F) around the intersection. At the end of the pre-construction period (February 1, 2022), cumulative subsidence at locations D, E, and F was 36.55 mm, 8.53 mm, and 31.75 mm, respectively. During construction period, subsidence trends at D and F persisted but

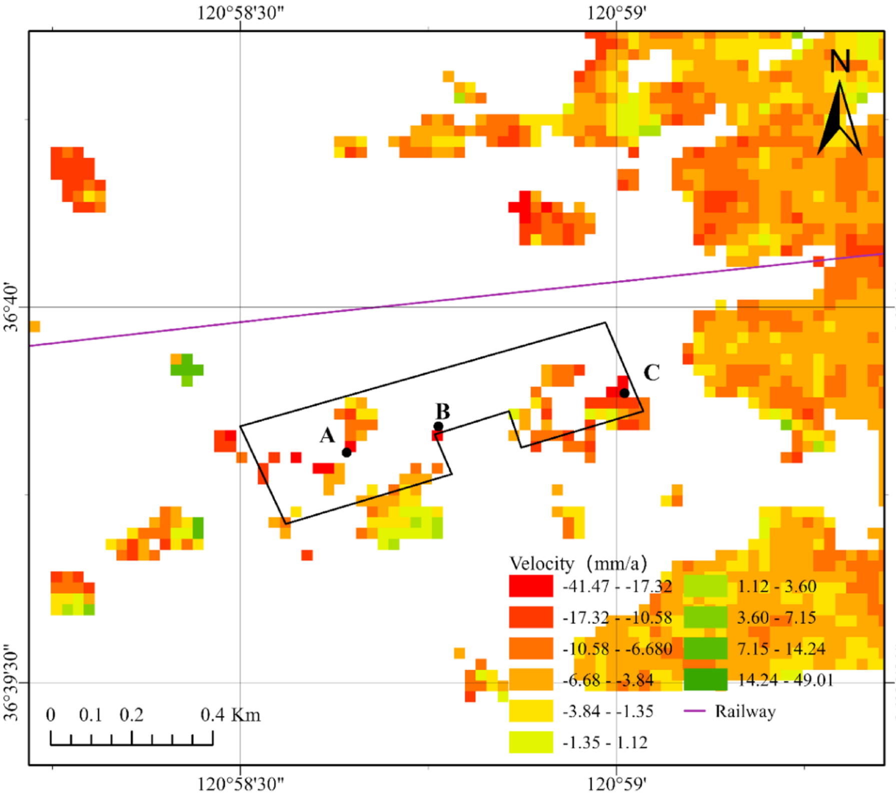

Fig. 12. Ground subsidence velocity map of Haiyang beam yard.

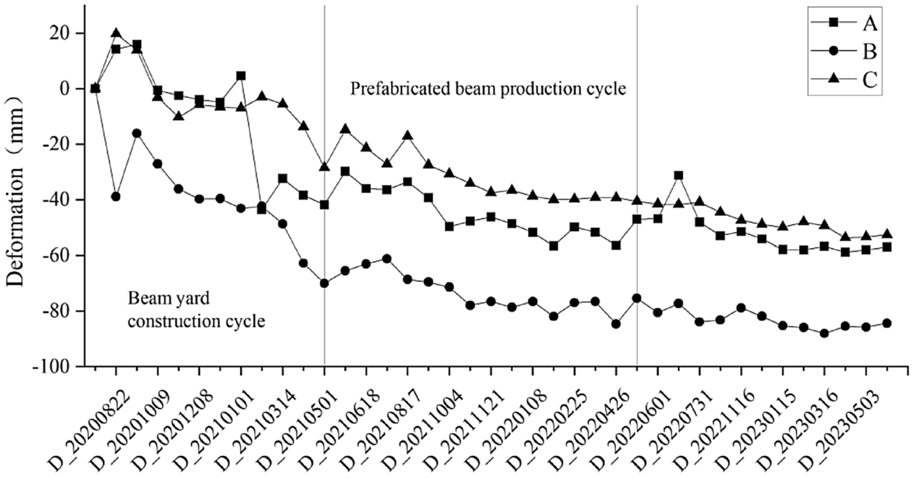

Fig. 13. Time series data of three locations in the Haiyang beam yard.

without significant acceleration in subsidence velocities, and Location F maintained the fluctuation pattern observed before construction.

Tunnel entrances and exits

Tunnel entrances and exits are critical for subsidence analysis due to their subgrade and slope engineering. The Tanshan Tunnel it located at Tuanwang Town, with its entrance at DK25 + 998 and exit at DK26 + 506, spanning 508 m. Figure 16 presents the subsidence velocities at the tunnel's entrance and exit. At the tunnel entrance, position G on the north side has a subsidence velocity of 13.81 mm/a, while at the exit, position H on the east side of the tunnel has a velocity of 7.54 mm/a.

Slope construction for the Tanshan Tunnel involved leveling (excavation and filling) followed by compaction. Figure 17 presents the time series subsidence data of position G at the tunnel entrance: Before leveling, cumulative

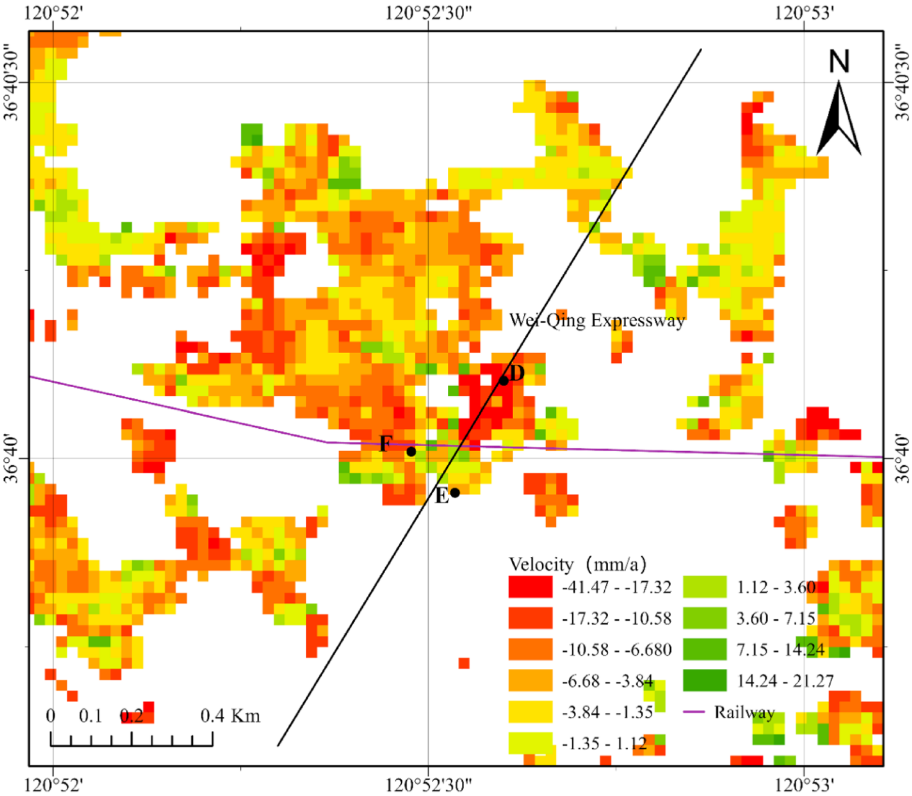

Fig. 14. Ground subsidence velocity map of the mega bridge over the Wei-Qing Expressway.

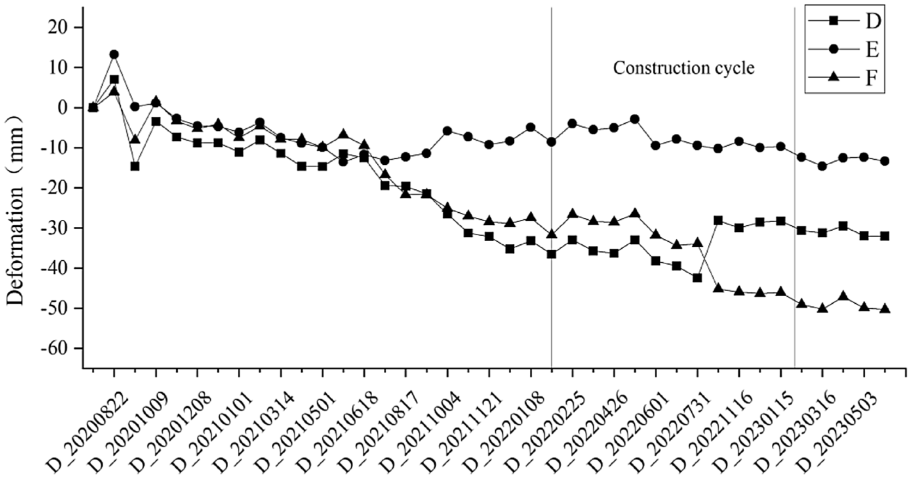

Fig. 15. Time series data of three locations near the Wei-Qing Expressway Grand Bridge.

subsidence at position G was negligible. During the leveling process, subsidence fluctuated. After compaction, cumulative subsidence at position G reached 41.95 mm.

Figure 18 presents the time series subsidence data of position H at the Tanshan Tunnel exit. Before compaction, cumulative subsidence at position H was negligible. During compaction, cumulative subsidence reached 24.42 mm. After track installation began, a ground uplift occurred, followed by a slow subsidence trend.

The Yingzishan Tunnel, located in Jiujia Village, Laiyang City, extends from DK34 + 728 to DK35 + 679, spanning 951 m. Figure 19 presents the subsidence velocity data for the Yingzishan Tunnel. At the tunnel entrance, position I on the north side has a subsidence velocity of 10.80 mm/a, and no valid SBAS-InSAR monitoring points were detected at the tunnel exit.

Position I, located at the top entrance of the slope, exhibited noticeable ground subsidence prior to November 2, 2020, with a cumulative subsidence amount of 12.03 mm, as shown in Fig. 20. Between November 2, 2020, and

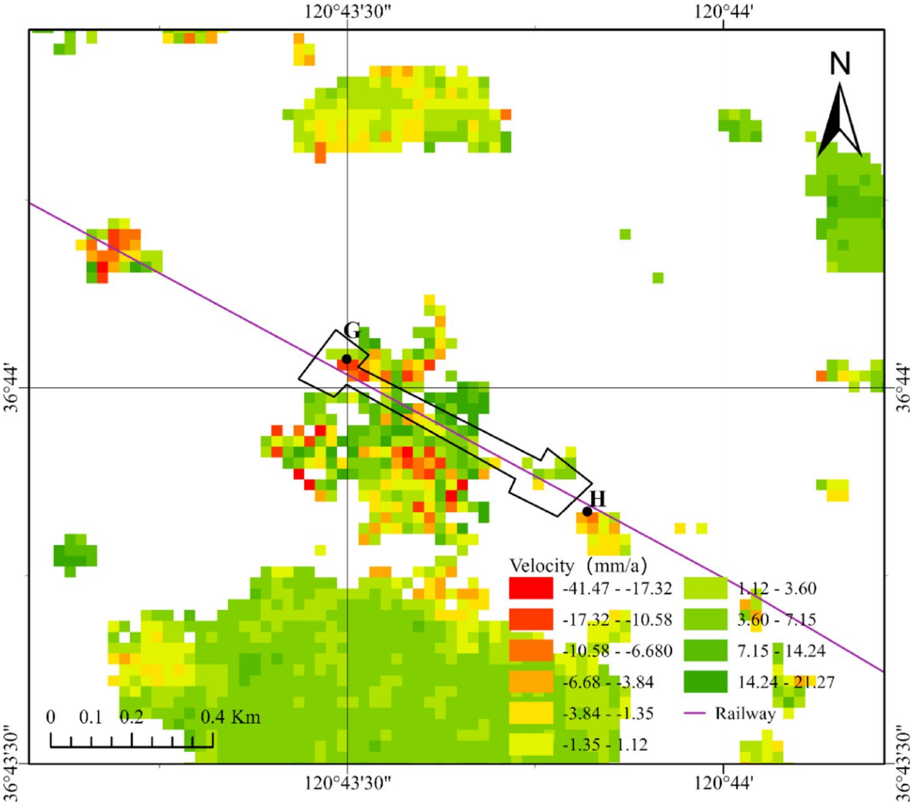

Fig. 16. Ground subsidence velocity map of Tanshan tunnel.

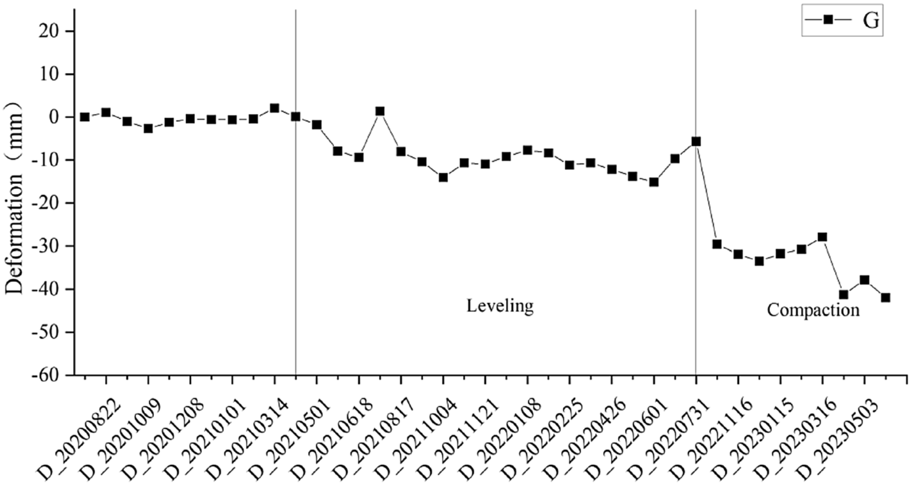

Fig. 17. Time series deformation at position G.

July 31, 2022, no significant subsidence trend was observed, although subsidence during this period displayed fluctuating variation. After slope backfilling and leveling commenced, the ground initially showed uplift, followed by significant subsidence. Then, the subsidence stabilized, indicating a transition to more stable ground conditions post-construction.

Discussion

Ground subsidence monitoring along railway using SBAS-InSAR

In this study, 39 Sentinel-1 A SAR images, acquired between July 2020 and May 2023, were processed to generate ground subsidence data along the Lairong High-Speed Railway. The SAR images cover the entire railway area and span from before the start of construction to after its completion, enabling the analysis of ground deformation

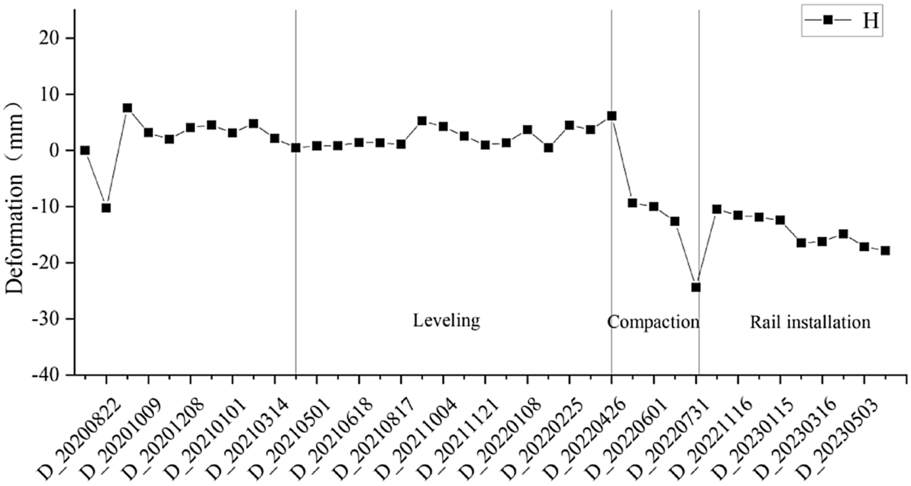

Fig. 18. Time series deformation at position H.

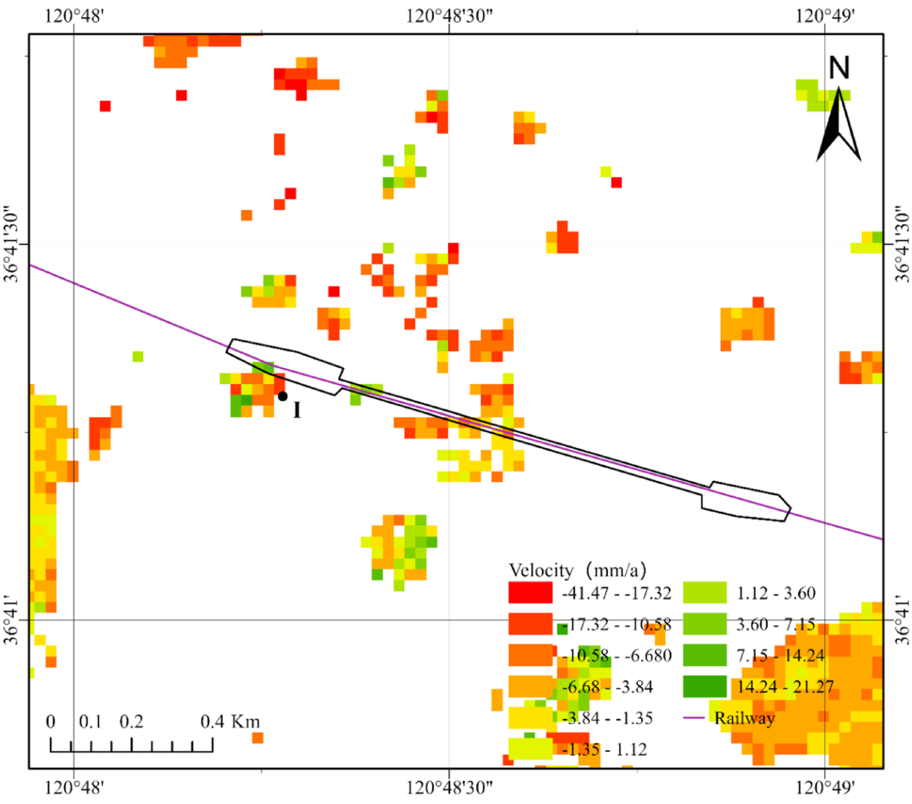

Fig. 19. Ground subsidence velocity map of Yingzishan tunnel.

patterns before and after construction to assess its impact. SBAS-InSAR, rather than PS-InSAR, was used because the railway was under construction, and its structure had not yet formed stable scatterers. Additionally, the area traversed by the railway is primarily covered by bare soil and vegetation, resulting in low ground reflection intensity, making SBAS-InSAR more suitable than PS-InSAR. In this study area, vegetation growth affects the overall coherence of interferometric pairs. In SBAS-InSAR data processing, some interferometric pairs with mean coherence less than 0.4 were removed to enhance the quality of data processing. Generally, a mean coherence of interferometric pairs above 0.4 is considered good, providing reliable deformation monitoring results[47]. The mean coherence coefficient of the SBAS-InSAR results within the 1-km buffer zone is 0.5, indicating that the SBAS-InSAR results can provide reliable ground deformation measurements.

Accurate ground subsidence data are essential for creating subsidence maps and performing subsequent time series analyses[48]. Therefore, thirty leveling points located within the SBAS-InSAR result pixels were selected to

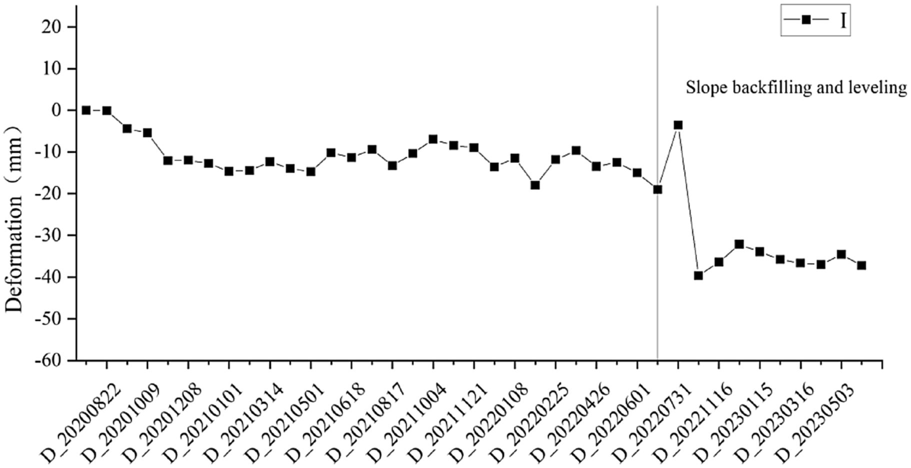

Fig. 20. Time series deformation at Position I.

validate the SBAS-InSAR results, with a maximum discrepancy of 8.79 mm and the RMSE of 3.84 mm, confirming the high precision of SBAS-InSAR for ground subsidence monitoring. However, the leveling measurement and SBAS-InSAR measurement results show significant differences at several locations, specifically DK25 + 426, DK41 + 374, and DK42 + 519, with absolute differences of 8.79 mm, 7.81 mm, and 7.74 mm, respectively, although they exhibit the same ground deformation trends (uplift or subsidence). It is noteworthy that these three locations are situated in areas with significant deformation compared to other leveling points. The possible reason for the difference is that the subsidence at a leveling point represents the deformation at that specific point, whereas the subsidence of an SBAS-InSAR pixel reflects the average ground subsidence within that pixel. This discrepancy can introduce potential errors during comparison, particularly due to geolocation mismatches between leveling points and InSAR pixels, as well as sub-pixel averaging effects. Using high-resolution SAR imagery can mitigate this issue. In practical engineering, the positioning accuracy of SBAS-InSAR results can be optimized by deploying corner reflectors along the railway. Continuous measurements of these artificial corner reflectors using GNSS can be conducted, and the resulting time-series deformation measurements can be used to validate the SBAS-InSAR results[49,50].

SBAS-InSAR technology is effective in monitoring large-scale infrastructure like railways, offering multiple advantages: it enables cost-effective and large-scale ground measurement[51], provides access to historical data[41], operates independently of weather conditions[52], and eliminates the need for ground-based measurement points. However, it also has certain limitations. The monitoring frequency depends on the satellite's revisit cycle. For instance, Sentinel-1 A has a standard revisit time of 12 days, but in this study, it was extended to 24 days to reduce computational load. This extension, however, limits the ability to capture rapid or nonlinear deformation events during active construction phases and may degrade the quality of interferograms due to the increased data interval. Additionally, temporal decorrelation of ground targets, caused by significant ground changes or coverage by vegetation and water bodies, can result in data loss. For example, in this study, SBAS-InSAR results were missing in some areas along the railway line. This spatial decorrelation primarily results from terrain undulations, variations in observation angles, and other environmental factors, which degrade interferogram quality and reduce the precision of surface deformation monitoring[53]. Finally, phase unwrapping errors, particularly in areas with low coherence or significant terrain variations, may lead to inaccuracies in the calculated deformation. Additionally, atmospheric effects, such as variations in tropospheric and ionospheric conditions, can further impact the accuracy of deformation measurements. Deformation maps should be interpreted in a relative context, as SBAS-InSAR measurements provide relative deformation values. Moreover, the absolute localization accuracy of the results is constrained by factors including orbit uncertainty, propagation delays, scattering center uncertainty, and atmospheric influences. To address these limitations, approaches such as applying DS-InSAR techniques or implementing atmospheric correction methods can increase the density and accuracy of time series InSAR results[54,55], thereby enhancing overall monitoring capabilities.

Spatiotemporal evolution of ground subsidence along the Lairong railway

The spatiotemporal evolution analysis of ground subsidence aims to determine the spatial distribution and temporal development patterns of subsidence. Hotspot analysis reveals that the DK30 ~ DK50 section experiences severe subsidence with significant clustering, and the mean cumulative subsidence time series for the buffer zone and this section was calculated and linearly fitted, showing continuous subsidence in both regions, with a higher rate in the DK30 ~ DK50 section. Throughout the monitoring period, the buffer zone exhibits increasing and fluctuating subsidence, while the DK30 ~ DK50 section consistently shows greater mean cumulative subsidence than the buffer zone.

The pronounced subsidence observed in the DK30 ~ DK50 section can be attributed to three primary factors. Optical image was used to generate using a base map in ArcGIS. First, its proximity to the coastline may increase subsidence rates, as coastal regions are generally more prone to elevated subsidence levels[56]. In previous studies, a similar pattern of ground subsidence distribution has been observed in Jiaozhou Bay, located less than 100 km from the current project site[57]. Second, there are several villages along the railway in this region, where high population density and surface loads from buildings, transportation, and infrastructure, significantly contribute to ground subsidence[58]. As shown in Fig. 21, the optical image illustrates the geographical locations of the railway, buildings, and roads along the DK30-DK50 section.

Third, ground deformation induced by large-scale tectonic activity is also a critical factor. As illustrated in Fig. 5, a substantial subsidence area extends across the engineering region in a northeast-southwest direction, with the DK30 ~ DK50 section located within this deformation zone. In previous studies, this ground surface deformation pattern has also been observed[59]. This section's pre-existing subsidence trend is evident, as significant subsidence was observed in both the buffer zone and the DK30–DK50 section before construction began on November 2, 2020. From the start of construction until July 2021, ground uplift was observed, followed by continuous subsidence in these regions as shown in Fig. 11. Time series MSC data for the entire study area were calculated and presented in Fig. 22, revealing a deformation pattern highly consistent with that of the buffer zone and the DK30–DK50 section, with minor differences during certain periods. However, the subsidence rate and magnitude in the DK30 ~ DK50 section were higher than those in the entire study area. Furthermore, after construction completion, cumulative subsidence in this section continued to increase, where it decreased in the entire study area and the buffer zone. Therefore, more attention should be given to DK30 ~ DK50 section during the operational phase to ensure its safety.

Time series deformation analysis at key railway nodes

Railway construction, typically spanning several years, involves multiple construction processes and phases across various structural components. Railway construction activities, such as the construction and beam fabrication at beam yards, the building of railway bridge piers, tunnel excavation[60], and track laying[61], can all cause ground subsidence. In these construction activities, excavation and backfilling can induce changes in surface elevation, while artificial preloading may lead to ground subsidence. Furthermore, the construction of railway facilities introduces additional ground loads, thereby triggering subsidence. Typically, excessive ground deformation occurring shortly after the start of construction is considered to be induced by construction activities. SBAS-InSAR technology offers substantial potential for monitoring time series deformation at key railway infrastructure, such as beam yards, bridges, and tunnel slopes, providing detailed and precise deformation data. In this study, SBAS-InSAR time series monitoring was utilized to assess subsidence development at significant locations along the Lairong Railway, including the Haiyang Beam Yard, the Wei-Qing Expressway Grand Bridge, and the entrances and exits of two tunnels.

The geological investigation report and borehole data outline the stratigraphy and properties of the subsurface layers at the site. The strata primarily consist of: (1) miscellaneous fill; (2) fully weathered granite; (3) strongly

Fig. 21. Geographic location and surface optical image of the DK30 ~ DK50 section. The Figure is generated by ArcGIS (https://www.esri.com/en-us/arcgis/products/arcgis-pro/resources).

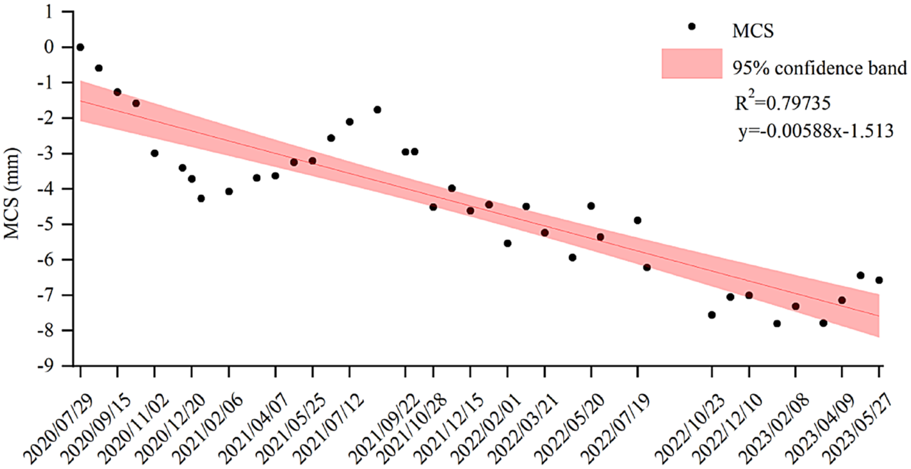

Fig. 22. Time series MSC of the study area.

Position	Monitoring period	r
A	2020.07.29 ~ 2021.07.12 and 2021.05.01 ~ 2022.04.26	0.8001
	2020.07.29 ~ 2021.07.12 and 2022.03.21 ~ 2023.05.27	0.5384
	2021.05.01 ~ 2022.04.26 and 2022.03.21 ~ 2023.05.27	0.6350
B	2020.07.29 ~ 2021.07.12 and 2021.05.01 ~ 2022.04.26	0.7336
	2020.07.29 ~ 2021.07.12 and 2022.03.21 ~ 2023.05.27	0.8495
	2021.05.01 ~ 2022.04.26 and 2022.03.21 ~ 2023.05.27	0.5775
C	2020.07.29 ~ 2021.07.12 and 2021.05.01 ~ 2022.04.26	0.7590
	2020.07.29 ~ 2021.07.12 and 2022.03.21 ~ 2023.05.27	0.7430
	2021.05.01 ~ 2022.04.26 and 2022.03.21 ~ 2023.05.27	0.8728

Table 4. Calculation results of self-correlation coefficient of point A, B and C.

weathered granite; (3 – 1) strongly weathered andesite; (4) moderately weathered granite; and (4 – 1) moderately weathered andesite. The deeper layers, such as the moderately weathered granite and andesite, exhibit higher strength and stability, while the upper miscellaneous fill is less stable due to its loose and heterogeneous composition. Consequently, the observed deformation during construction is predominantly attributed to the compression and settlement of the miscellaneous fill layer[62]. Given the inherent instability of the miscellaneous fill layer, the short-term deformation observed at the site is primarily driven by its compression and settlement, with construction activities acting as a significant catalyst that accelerates this process.

The ground deformation velocity map of the Haiyang Beam Yard indicates that the subsidence velocity within the yard significantly exceeds that of surrounding areas. Additionally, SBAS-InSAR time series subsidence results from three locations within the beam yard exhibited pronounced subsidence during construction, accompanied by significant fluctuations, and the subsidence values were far greater than the mean subsidence value of the entire study area. Table 4 presents the correlation coefficients of the time series deformation data for points A, B, and C across different time periods: the construction phase (2020.07.29 ~ 2021.07.12), the prefabricated beam production phase (2021.05.01 ~ 2022.04.26), and the post-production phase (2022.03.21 ~ 2023.05.27). The correlation coefficients indicate that the deformation patterns of points A, B, and C exhibit relatively similar trends across the three phases: construction, beam production, and post-production. However, the correlation coefficients are relatively low for specific stages, except for beam yard construction and beam production stages at point A (0.5384) and beam production and post-production stages at point B (0.5775).

At the Wei-Qing Expressway Grand Bridge, the subsidence velocity at the railway-expressway intersection was significantly higher than in surrounding areas, indicating localized subsidence. Time series data from points D, E, and F reveal distinct deformation patterns: points D and F exhibited continuous subsidence throughout the monitoring period, whereas point E showed minimal subsidence. Notably, between July 31, 2022, and October 23, 2022, points D and F underwent significant deformation, with point D uplifting by 14.3 mm and point F subsiding by 11.3 mm.

The monitoring period is divided into two phases: February 6, 2021, to February 1, 2022, representing the year before construction, and February 1, 2022, to April 9, 2023, covering the construction phase and a period after its completion. Table 5 presents the correlation coefficients of deformation for points D, E, and F during these two phases, which are – 0.6207, −0.3399, and 0.9301, respectively. The results show that the deformation patterns of points D and E changed significantly compared to the pre-construction period, while point F's deformation pattern remained relatively consistent. By examining changes in the correlation coefficients of

Position	Monitoring period	r
D	2021.02.06 ~ 2022.02.01 and 2022.02.01 ~ 2023.04.09	−0.6207
E	2021.02.06 ~ 2022.02.01 and 2022.02.01 ~ 2023.04.09	−0.3399
F	2021.02.06 ~ 2022.02.01 and 2022.02.01 ~ 2023.04.09	0.9301

Table 5. Calculation results of self-correlation coefficient of point D, E and F.

time series deformation data between these phases, the impact of construction activities on these points can be assessed, indicating that points D and E were likely influenced by the construction process.

The subsidence map of the tunnel entrances and exits indicates a greater susceptibility to subsidence at slope locations and subgrade sections. Time series deformation data from three points near the tunnel entrances and exits reveal that, upon the start of construction activities, deformation exhibited significant changes, with ground leveling frequently causing fluctuating ground elevation and compaction consistently leading to pronounced subsidence.

By leveraging high-precision time series deformation monitoring, SBAS-InSAR enables the analysis of the temporal evolution of subsidence at specific points across various construction stages. By examining changes in the correlation coefficients of time series deformation data between these stages, the impact of construction activities on these points can be assessed. Furthermore, combining time series analysis with construction process data provides deeper insights into subsidence development, including its timing and causes. Comparing subsidence rates and cumulative amounts before, during, and after construction facilitates the identification of specific construction impacts and affected locations. This approach supports timely interventions and adjustments to construction processes, minimizing the risk of further subsidence and enhancing railway operational safety.

Conclusions

The novelty of this study is demonstrated through the innovative application of hotspot analysis to characterize the spatial distribution and clustering of subsidence along railway lines, coupled with a sensitivity analysis for selecting the optimal fixed-band distance based on Chinese railway standards. Furthermore, SBAS-InSAR time-series deformation data are integrated with construction processes at critical structural locations, such as beam yards, tunnel entrances, and bridge piers, to identify construction-induced subsidence. Sudden changes in subsidence rates are detected immediately following the initiation of construction activities, providing empirical evidence of anthropogenic influences. Additionally, changes in subsidence patterns across different construction phases are quantified using correlation coefficients between time-series deformations, enabling the differentiation of construction-related effects from natural geological processes. This approach not only enhances the precision of subsidence monitoring in railway engineering but also offers a robust framework for validating deformation sources,

First, SBAS-InSAR offers several advantages for railway subsidence monitoring, including access to historical data, low costs, and millimeter-level accuracy, which effectively complement traditional ground leveling methods. However, it faces limitations in detecting deformations in areas with excessive ground movement or low-coherence regions covered by vegetation, while satellite revisit cycles constrain high-frequency monitoring. These challenges can be mitigated by deploying artificial corner reflectors and GNSS stations along the railway to validate SBAS-InSAR results and optimize geolocation accuracy. Additionally, utilizing high-resolution SAR imagery and integrating DS-InSAR techniques can enhance detection density in low-coherence areas.

Second, combining SBAS-InSAR with hotspot analysis enables efficient identification of subsidence spatial distribution and clustering zones along the railway. Additionally, SBAS-InSAR time series data tracks deformation at key locations, and by integrating construction processes, timelines, and correlation analysis, the deformation patterns and the impact of construction activities on specific locations can be assessed.

Finally, large-scale crustal deformation significantly affects the Lai-Rong Railway, with the DK30 ~ DK50 section experiencing notably higher subsidence. This section requires increased monitoring frequency during construction and operation to ensure safety. Construction activities such as excavation, leveling, subgrade compaction, and introduced loads (e.g., precast beams and vehicles) drive surface fill soil deformation, a primary cause of ground subsidence. Thorough compaction of fill layers during construction is recommended to mitigate long-term subsidence risks.

Data availability

The data that support the findings of this study are available from the corresponding author upon reasonable request.

Received: 8 February 2025; Accepted: 16 September 2025

References

1. Changming, L., Jingjie, Y. & Kendy, E. Groundwater exploitation and its impact on the environment in the North China plain. *Water Int.* **26**, 265–272 (2001).
2. Guo, H. et al. Groundwater-derived land subsidence in the North China plain. *Environ. Earth Sci.* **74**, 1415–1427 (2015).

3. Su, G. et al. Spatiotemporal evolution characteristics of land subsidence caused by groundwater depletion in the North China plain during the past six decades. *J. Hydrol.* **600**, 126678 (2021).
4. Kaewunruen, S. & Xu, N. Digital twin for sustainability evaluation of railway station buildings. *Front. Built Environ.* **4**, 77 (2018).
5. Kaewunruen, S., AbdelHadi, M., Kongpuang, M., Pansuk, W. & Remennikov, A. M. Digital twins for managing railway Bridge maintenance, resilience, and climate change adaptation. *Sensors* **23**, 252 (2022).
6. Remennikov, A. M. & Kaewunruen, S. A review of loading conditions for railway track structures due to train and track vertical interaction. *Struct. Control Health Monitoring: Official J. Int. Association Struct. Control Monit. Eur. Association Control Struct.* **15**, 207–234 (2008).
7. Shi, Y., Li, M., Chen, J. & Wang, J. Long-term settlement behavior of a highway in land subsidence area. *J. Perform. Constr. Facil.* **32**, 04018063 (2018).
8. Yau, J. Response of a train moving on multi-span railway bridges undergoing ground settlement. *Eng. Struct.* **31**, 2115–2122 (2009).
9. Ge, L. et al. Impact of ground subsidence on the Beijing–Tianjin high-speed railway as mapped by radar interferometry. *Ann. GIS.* **16**, 91–102 (2010).
10. Yan, B., Dai, G. L. & Hu, N. Recent development of design and construction of short span high-speed railway bridges in China. *Eng. Struct.* **100**, 707–717 (2015).
11. Wang, Y., Liang, S., Huang, C. & Wang, R. Foundation settlement response of existing high-speed railway Bridge induced by construction of undercrossing roads. *Sustainability* **14**, 8700 (2022).
12. GuangYao, D. et al. Monitoring and analysis of land subsidence along Beijing-Tianjin inter-city railway. *J. Indian Soc. Remote Sens.* **44**, 915–931 (2016).
13. Liu, C., Li, N., Wu, H. & Meng, X. Detection of high-speed railway subsidence and geometry irregularity using terrestrial laser scanning. *J. Surv. Eng.* **140**, 04014009 (2014).
14. Chang, C. & Wang, T. GPS monitoring ground subsidence associated with seasonal underground water level decline: case analysis for a section of Taiwan high speed rail. *Surveying Land. Inform. Sci.* **66**, 45–54 (2006).
15. Graham, L. C. Synthetic interferometer radar for topographic mapping. *Proceedings of the IEEE* 62, 763–768 (1974).
16. Gabriel, A. K., Goldstein, R. M. & Zebker, H. A. Mapping small elevation changes over large areas: differential radar interferometry. *J. Geophys. Research: Solid Earth.* **94**, 9183–9191 (1989).
17. Hu, J. et al. 3D coseismic displacement of 2010 Darfield, new Zealand earthquake estimated from multi-aperture InSAR and D-InSAR measurements. *J. Geodesy.* **86**, 1029–1041 (2012).
18. Schlögel, R., Doubre, C., Malet, J. P. & Masson, F. Landslide deformation monitoring with ALOS/PALSAR imagery: A D-InSAR Geomorphological interpretation method. *Geomorphology* **231**, 314–330 (2015).
19. Hu, Z. & Mallorquí, J. J. An accurate method to correct atmospheric phase delay for Insar with the era5 global atmospheric model. *Remote Sens.* **11**, 1969 (2019).
20. Ferretti, A., Prati, C. & Rocca, F. Permanent scatterers in SAR interferometry. *IEEE Trans. Geosci. Remote Sens.* **39**, 8–20. https://doi.org/10.1109/36.898661 (2001).
21. Berardino, P., Fornaro, G., Lanari, R. & Sansosti, E. A new algorithm for surface deformation monitoring based on small baseline differential SAR interferograms. *IEEE Trans. Geosci. Remote Sens.* **40**, 2375–2383 (2002).
22. Chen, B. et al. Characterization and causes of land subsidence in Beijing, China. *Int. J. Remote Sens.* **38**, 808–826 (2017).
23. Zhou, C. et al. Enhanced dynamic landslide hazard mapping using MT-InSAR method in the three Gorges reservoir area. *Landslides* **19**, 1585–1597 (2022).
24. Galve, J. P. et al. Evaluation of the SBAS InSAR service of the European space agency's geohazard exploitation platform (GEP). *Remote Sens.* **9**, 1291 (2017).
25. Rodríguez-Antuñano, I. et al. Empowering intermediate cities: cost-effective heritage preservation through satellite remote sensing and deep learning. *Int. J. Remote Sens.* **45**, 4046–4074 (2024).
26. Rodríguez-Antuñano, I., Martínez-Sánchez, J., Lagüela-López, S. & Riveiro, B. Towards more resilient smart cities: Mt-insar monitoring of urban infrastructure using machine learning techniques. *ISPRS Annals Photogrammetry Remote Sens. Spat. Inform. Sci.* **10**, 221–228 (2022).
27. Rodríguez-Antuñano, I., Martínez-Sánchez, J., Cabaleiro, M. & Riveiro, B. Anticipating the collapse of urban infrastructure: a methodology based on Earth observation and MT-InSAR. *Remote Sens.* **15**, 3867 (2023).
28. Gao, M. et al. Land subsidence and ground fissures in Beijing capital international airport (bcia): evidence from quasi-ps Insar analysis. *Remote Sens.* **11**, 1466 (2019).
29. D'Amico, F., Gagliardi, V., Ciampoli, L. B. & Tosti, F. Integration of InSAR and GPR techniques for monitoring transition areas in railway bridges. *NDT E Int.* **115**, 102291 (2020).
30. Lyu, M. et al. Detection of seasonal deformation of highway overpasses using the PS-InSAR technique: A case study in Beijing urban area. *Remote Sens.* **12**, 3071 (2020).
31. Zhang, Q., Li, Y., Zhang, J. & Luo, Y. InSAR technique applied to the monitoring of the Qinghai–Tibet railway. *Nat. Hazards Earth Syst. Sci.* **19**, 2229–2240 (2019).
32. Shami, S., Azar, M. K., Nilfouroushan, F., Salimi, M. & Reshadi, M. A. M. Assessments of ground subsidence along the railway in the Kashan plain, Iran, using Sentinel-1 data and NSBAS algorithm. *Int. J. Appl. Earth Obs. Geoinf.* **112**, 102898 (2022).
33. Zhou, L. et al. Deformation monitoring of long-span railway bridges based on SBAS-InSAR technology. *Geodesy Geodyn.* **15**, 122–132 (2024).
34. Zhang, J., Zhu, W., Cheng, Y. & Li, Z. Landslide detection in the linzhi–ya'an section along the sichuan–tibet railway based on InSAR and hot spot analysis methods. *Remote Sens.* **13**, 3566 (2021).
35. Lu, B. et al. Study on InSAR deformation information extraction and stress state assessment in railway tunnel in plateau area. *Front. Earth Sci.* **12**, 1367978 (2024).
36. Tao, R. et al. Monitoring of ground displacement-induced railway anomalies using PS-InSAR techniques. *Measurement* **248**, 116863 (2025).
37. Chang, L., Dollevoet, R. & Hanssen, R. Railway infrastructure monitoring using satellite radar data. *Int. J. Railw Technol.* **3**, 79–91 (2014).
38. Hu, F., Leijen, F. J., Chang, L., Wu, J. & Hanssen, R. F. Monitoring deformation along railway systems combining multi-temporal InSAR and lidar data. *Remote Sens.* **11**, 2298 (2019).
39. Koohmishi, M., Kaewunruen, S., Chang, L. & Guo, Y. Advancing railway track health monitoring: integrating GPR, InSAR and machine learning for enhanced asset management. *Autom. Constr.* **162**, 105378 (2024).
40. Jin, B. et al. Susceptibility analysis of land subsidence along the transmission line in the salt lake area based on remote sensing interpretation. *Remote Sens.* **14**, 3229 (2022).
41. Li, S., Xu, W. & Li, Z. Review of the SBAS InSAR Time-series algorithms, applications, and challenges. *Geodesy Geodyn.* **13**, 114–126 (2022).
42. Asuero, A. G., Sayago, A. & González, A. The correlation coefficient: an overview. *Crit. Rev. Anal. Chem.* **36**, 41–59 (2006).
43. Lee, S. J., Yun, H. S. & Kwak, S. W. Sustainable risk mapping of High-Speed rail networks through PS-InSAR and Geospatial analysis. *Sustainability* **17**, 7064 (2025).
44. Wang, Y. et al. Using TerraSAR X-band and sentinel-1 C-band SAR interferometry for deformation along Beijing-Tianjin intercity railway analysis. *IEEE J. Sel. Top. Appl. Earth Observations Remote Sens.* **14**, 4832–4841 (2021).

45. Chen, M. et al. Land subsidence-induced damage assessment along Beijing–Tianjin high-speed railway from space using high-resolution TerraSAR-X data. *Struct. Health Monit.* https://doi.org/10.1177/14759217251334328 (2025).
46. National Railway Administration of China. Code for design of High-Speed Railway, TB10621-2014. *China Railway Publishing House: Beijing China*, (2014). (in Chinese).
47. Guo, J. et al. Study on optimization method for InSAR baseline considering changes in vegetation coverage. *Sensors* **24**, 4783 (2024).
48. Chai, L., Xie, X., Wang, C., Tang, G. & Song, Z. Ground subsidence risk assessment method using PS-InSAR and lightgbm: a case study of Shanghai metro network. *Int. J. Digit. Earth*. **17**, 2297842 (2024).
49. Czikhardt, R., Van Der Marel, H. & Papco, J. G. E. C. O. R. I. S. An open-source toolbox for analyzing time series of corner reflectors in InSAR geodesy. *Remote Sens.* **13**, 926 (2021).
50. Yeh, T. K. et al. Combination on GNSS precise point positioning and InSAR data fusion to monitor the land subsidence in Taiwan. *Geomatics Nat. Hazards Risk*. **16**, 2445632 (2025).
51. Tao, Q., Guo, Z., Wang, F., An, Q. & Han, Y. SBAS-InSAR time series ground subsidence monitoring along metro line 13 in Qingdao, China. *Arab. J. Geosci.* **14**, 1–14 (2021).
52. Li, R., Gong, X., Zhang, G. & Chen, Z. Wide-Area subsidence monitoring and analysis using Time-Series InSAR technology: A case study of the Turpan basin. *Remote Sens.* **16**, 1611 (2024).
53. Lee, H. & Liu, J. G. in *IEEE 1999 International Geoscience and Remote Sensing Symposium. IGARSS'99 (Cat. No. 99CH36293).* 485–487 (IEEE).
54. Bai, Z., Wang, Y. & Balz, T. Beijing land subsidence revealed using PS-InSAR with long time series TerraSAR-X SAR data. *Remote Sens.* **14**, 2529 (2022).
55. Liu, Y., Yang, H., Wang, S., Xu, L. & Peng, J. Monitoring and stability analysis of the deformation in the Woda landslide area in Tibet, China by the DS-InSAR method. *Remote Sens.* **14**, 532 (2022).
56. Yin, P. et al. Coastal erosion in Shandong of china: status and protection challenges. *China Geol.* **1**, 512–521 (2018).
57. Tao, Q. et al. Land subsidence monitoring and analysis in Qingdao, China using time series InSAR combining PS and DS. *Geomatics Nat. Hazards Risk*. **16**, 2447543 (2025).
58. Souza, W. O. et al. Analysis of Urbanization-Induced land subsidence in the City of Recife (Brazil) using persistent scatterer SAR interferometry. *Remote Sens.* **16**, 2592 (2024).
59. Li, F., Liu, G., Gong, H., Chen, B. & Zhou, C. Assessing land subsidence-inducing factors in the Shandong Province, China, by using PS-InSAR measurements. *Remote Sens.* **14**, 2875 (2022).
60. Niu, G., He, X., Xu, H. & Dai, S. Tunnelling-induced ground surface settlement: A comprehensive review with particular attention to artificial intelligence technologies. *Nat. Hazards Res.* **4**, 148–168 (2024).
61. Powrie, W. Soil mechanics principles for modelling railway track performance. *Transp. Geotechnics*. **47**, 101265 (2024).
62. Zhou, S., Wang, B. & Shan, Y. Review of research on high-speed railway subgrade settlement in soft soil area. *Railway Eng. Sci.* **28**, 129–145 (2020).

Acknowledgements

The authors sincerely thank the European Space Agency (ESA) for providing the sentinel- 1A SAR images. The authors thank the National Aeronautics and Space Administration (NASA) for providing the DEM data.

Author contributions

F.S. and L.C. conceptualized the study and designed the methodology. L.C. and J.W. developed the software. Validation was performed by F.S., J.W., and X.Z. The investigation was conducted by X.Z. and L.M. The original draft was prepared by L.C. and K.G., while L.C. and X.X. reviewed and edited the manuscript. L.C. and Q.H. were responsible for visualization. Supervision was carried out by F.S. and X.X. Project administration was managed by F.S. and XQ.Z. Funding acquisition was led by XQ.Z. All authors reviewed and approved the final manuscript version.

Funding

This research was funded by Research on Key Technologies for Green and Intelligent Construction of High-Speed Railways, grant number kh0160020230946; Science and Technology Council of Shanghai, grant number No.22dz1208500.

Declarations

Competing interests

The authors declare no competing interests.

Additional information

Correspondence and requests for materials should be addressed to X.Z.